Composition-dependent thermodynamics of intracellular phase separation

https://doi.org/10.1038/s41586-020-2256-2

Received: 10 October 2019

Accepted: 1 April 2020

Published online: 06 May 2020

Check for updates

Joshua A. Riback[1,6], Lian Zhu[1,6], Mylene C. Ferrolino[2], Michele Tolbert[2], Diana M. Mitrea[2,5], David W. Sanders[1], Ming-Tzo Wei[1], Richard W. Kriwacki[2]✉ & Clifford P. Brangwynne[1,3,4]✉

Intracellular bodies such as nucleoli, Cajal bodies and various signalling assemblies represent membraneless organelles, or condensates, that form via liquid–liquid phase separation (LLPS)[1,2]. Biomolecular interactions—particularly homotypic interactions mediated by self-associating intrinsically disordered protein regions—are thought to underlie the thermodynamic driving forces for LLPS, forming condensates that can facilitate the assembly and processing of biochemically active complexes, such as ribosomal subunits within the nucleolus. Simplified model systems[3–6] have led to the concept that a single fixed saturation concentration is a defining feature of endogenous LLPS[7–9], and has been suggested as a mechanism for intracellular concentration buffering[2,7,8,10]. However, the assumption of a fixed saturation concentration remains largely untested within living cells, in which the richly multicomponent nature of condensates could complicate this simple picture. Here we show that heterotypic multicomponent interactions dominate endogenous LLPS, and give rise to nucleoli and other condensates that do not exhibit a fixed saturation concentration. As the concentration of individual components is varied, their partition coefficients change in a manner that can be used to determine the thermodynamic free energies that underlie LLPS. We find that heterotypic interactions among protein and RNA components stabilize various archetypal intracellular condensates—including the nucleolus, Cajal bodies, stress granules and P-bodies—implying that the composition of condensates is finely tuned by the thermodynamics of the underlying biomolecular interaction network. In the context of RNA-processing condensates such as the nucleolus, this manifests in the selective exclusion of fully assembled ribonucleoprotein complexes, providing a thermodynamic basis for vectorial ribosomal RNA flux out of the nucleolus. This methodology is conceptually straightforward and readily implemented, and can be broadly used to extract thermodynamic parameters from microscopy images. These approaches pave the way for a deeper understanding of the thermodynamics of multicomponent intracellular phase behaviour and its interplay with the nonequilibrium activity that is characteristic of endogenous condensates.

To determine the thermodynamics of LLPS for intracellular condensates, we first focused on the liquid granular component of nucleoli within HeLa cells—in particular on the protein nucleophosmin (NPM1), which is known to be a key driver of nucleolar phase separation[11,12]. Under typical endogenous expression levels, we estimate the concentration of NPM1 in the nucleoplasm (C^{dil}) to be approximately 4 μM; from simple binary phase separation models (regular solution theory)[13] (Supplementary Note 1), this apparent saturation concentration, C_{sat}, is expected to be fixed even under varied protein expression levels (Fig. 1c). Consistent with previous studies[11], the overexpression of NPM1 resulted in larger nucleoli, underscoring the importance of NPM1 in nucleolar assembly (Fig. 1a). However, with these increased levels of NPM1, the nucleoplasmic concentration did not remain fixed at a single C_{sat}, but instead increased by roughly tenfold (Fig. 1b, Supplementary Note 2). Notably, the concentration of NPM1 within the dense-phase nucleolus, C^{den}, also increased, but the ratio of the dense-phase to dilute-phase concentrations, known as the partition coefficient $K = \frac{C^{\mathrm{den}}}{C^{\mathrm{dil}}}$, decreased considerably (Extended Data Fig. 1).

To elucidate the underlying biophysics of this non-fixed C_{sat} within living cells, we examined the phase separation of model biomimetic condensates that are not native within the cell. Using the optoDroplet system[4] developed for controlling intracellular phase separation, we fused the blue-light-dependent higher-order oligomerizing protein Cry2 to the intrinsically disordered region of DDX4, which drives the

[1]Department of Chemical and Biological Engineering, Princeton University, Princeton, NJ, USA. [2]Department of Structural Biology, St Jude Children's Research Hospital, Memphis, TN, USA. [3]Lewis Sigler Institute for Integrative Genomics, Princeton University, Princeton, NJ, USA. [4]Howard Hughes Medical Institute, Princeton University, Princeton, NJ, USA. [5]Present address: Dewpoint Therapeutics, Boston, MA, USA. [6]These authors contributed equally: Joshua A. Riback, Lian Zhu. ✉e-mail: richard.kriwacki@stjude.org; brangwy@princeton.edu

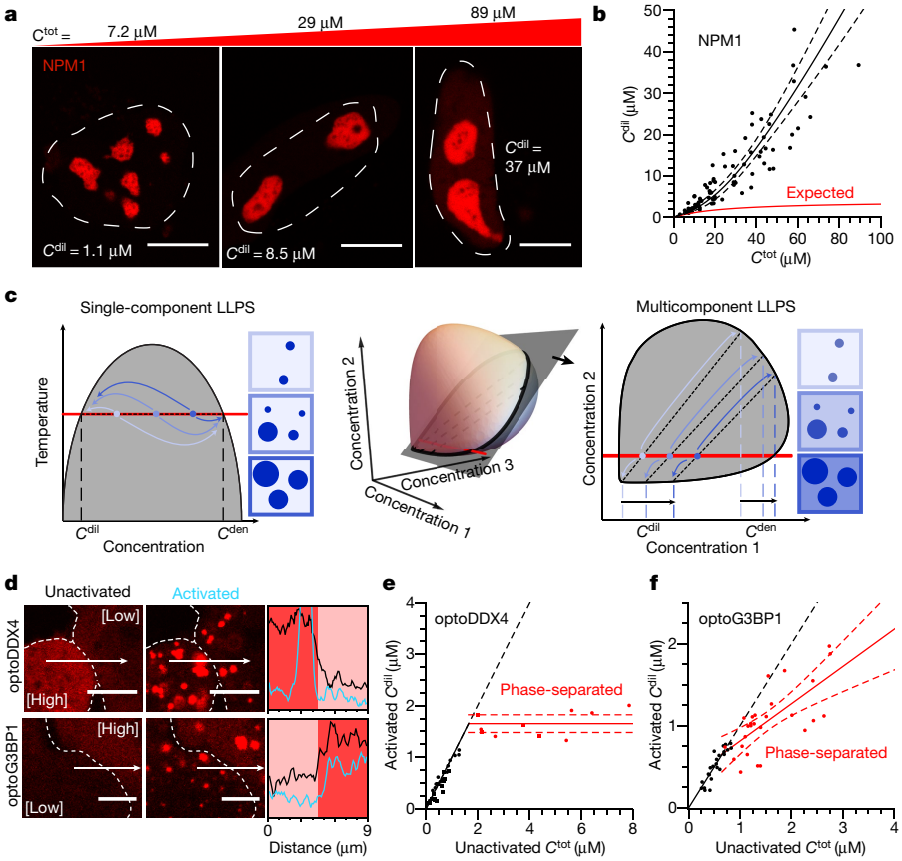

Fig. 1 | Multicomponent LLPS results in non-fixed C_{sat} and the emergence of a concentration-dependent phase stability. a, Example images of cells (from $n = 79$ cells) expressing NPM1–mCherry. The total nuclear concentration (C^{tot}) and nucleoplasmic concentration (C^{dil}) of NPM1–mCherry is shown at top of the image and within the image, respectively. The white dashed lines denote the nuclear boundary as defined by NPM1. Scale bars, 10 µm. **b**, The concentration of NPM1–mCherry in the nucleoplasm (C^{dil}) with respect to the total NPM1–mCherry concentration in the nucleus (C^{tot}). The expected trend for a single C_{sat} is shown in red. **c**, Graphical representation of phase diagrams for both single-component (left) and multicomponent (right) LLPS showing fixed and non-fixed C^{dil} (or C_{sat}), respectively. Component concentration changes along the red line; within the grey-shaded region, molecules separate into two phases in which concentrations (curved arrows) are defined by the dashed tie lines. For a multicomponent system, the two-dimensional phase diagram is a slice of a higher dimensional one, resulting in skewed tie lines and non-fixed C_{sat}. **d**, Example images of cells expressing optoDroplet constructs with optoDDX4 (top, from $n = 19$ cells) or optoG3BP1 (bottom, from $n = 49$ cells), before (left) and after (right) full activation. The line scans shown on the far right correspond to intensity traces before (black) and after (blue) activation. **e**, **f**, Quantification of optoDroplet constructs with optoDDX4 (**e**) and with optoG3BP1 (**f**). The circles represent cytoplasmic concentrations and the squares represent nucleoplasmic concentrations. Cells shown as red points exhibit condensates upon activation (none had condensates before activation); dashed lines represent the mean confidence intervals for cells with foci for constant and linear fits in optoDDX4 and optoG3BP1, respectively. OptoG3BP1 experiments are arsenite-stressed cells in which G3BP1A and G3BP1B are knocked out; optoDDX4 data are reproduced from ref. [14]. Scale bars, 5 µm.

phase separation of exogenous condensates through predominately homotypic interactions[3,4,10]. Consistent with previous work[14], at total cellular concentrations greater than about 1.7 µM, light activates droplet formation and the nucleoplasmic and cytoplasmic C^{dil} remains at a fixed value, suggesting a fixed C_{sat} of approximately 1.7 µM (Fig. 1d, e). We next asked whether a fixed C_{sat} would be observed upon light induction of stress granules (multicomponent, stress-inducible condensates that assemble through heterotypic protein–mRNA interactions[15]). We replaced the oligomerization domain of G3BP1—a critical stress granule protein—with Cry2, and expressed this construct in G3BP1/G3BP2 knockout cells under arsenite stress. At total cytoplasmic concentrations greater than about 0.7 µM, light triggered droplet formation; however, unlike in the case of synthetic DDX4, the C^{dil} was not fixed but instead increased with increasing total concentrations (Fig. 1d, f), similar to the behaviour of NPM1 (Fig. 1a, b). These results are not restricted to light-induced oligomerization of G3BP1 using the optogenetic system, as increasing expression of G3BP1 in a G3BP1/G3BP2 knockout cell line results in a similar increase in the C^{dil} (Extended Data Fig. 2a).

These data suggest that multicomponent condensates are not governed by a fixed C_{sat}, as would be expected for a single-biomolecule-component (that is, binary solution when including the solvent) (Supplementary Note 1) phase boundary at fixed temperature. Instead, endogenous condensates may be governed by the more richly textured thermodynamics that dictate higher-dimensional phase diagrams (Fig. 1c), consistent with theoretical and experimental findings on model multicomponent systems[13,16–22]. To investigate this concentration-dependent thermodynamics, we quantify the effect of increasing the concentration of a biomolecule in vivo or in vitro, which shifts the stoichiometry to bias towards more homotypic interactions (Fig. 2a, Extended Data Fig. 3, Supplementary Note 3). This changes the partition coefficient, enabling us to quantify changes in the generalized standard free energy of transfer, here denoted as ΔG^{tr}, for any component from the dilute to the dense phase (Fig. 2b); thermodynamic considerations yield the relationship $\Delta G^{tr} = -RT \ln K$ (Supplementary Note 4). For components that contribute to phase separation (for example, those that act to scaffold the condensate

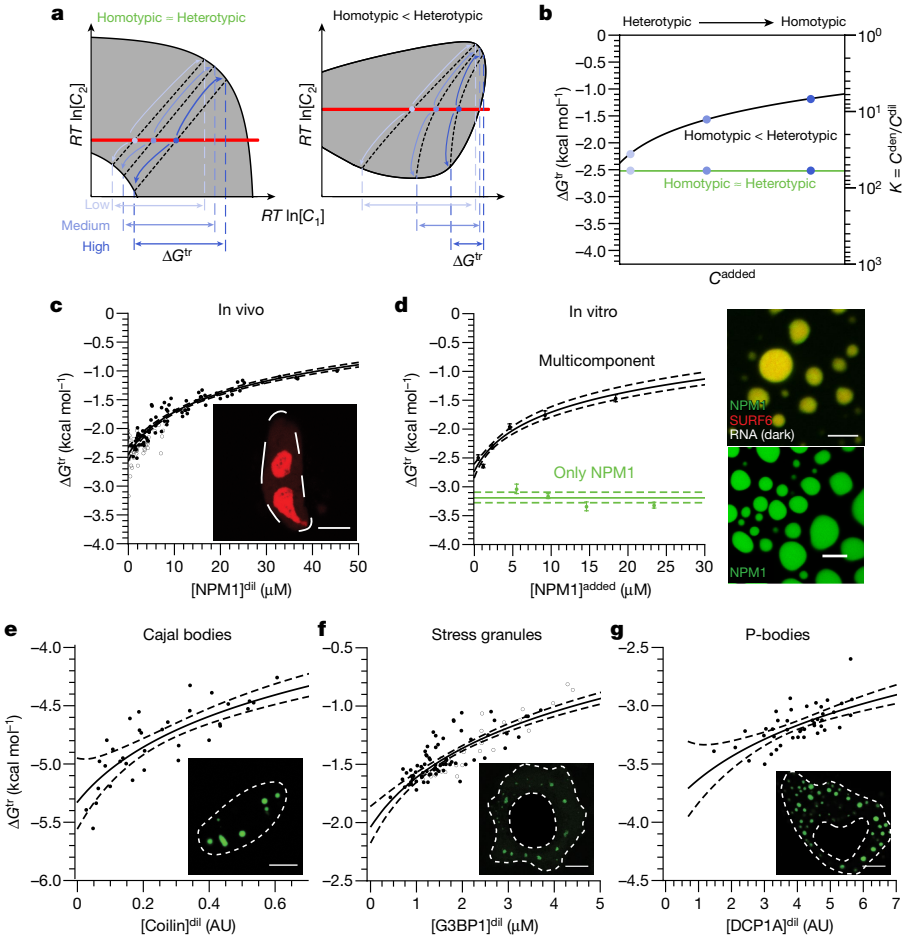

Fig. 2 | Determining the contribution of heterotypic and homotypic interactions that drive condensate formation in vivo and in vitro. **a**, Schematic of the connection between the phase diagram and the transfer free energy of a component when heterotypic interactions are equal to (left) or stronger than (right) homotypic interactions. C_1 and C_2 represent components 1 and 2. **b**, Accompanying schematic to **a**, detailing the qualitative change in the transfer free energy of component 1 with an increase in its expression for the two cases in **a**. **c**, Thermodynamic dependence of NPM1 (−mCherry filled, −GFP empty) transfer from the nucleoplasm into the nucleolus, as a function of its increased expression (concentration in the nucleoplasm). The inset is an image from Fig. 1a, to highlight that these data represent a reanalysis of those experiments. **d**, Left, ΔG^{tr} for NPM1 as a function of added NPM1, obtained from in vitro reconstitution experiments. Right, images of NPM1 droplets with 5% PEG (bottom) and of ternary NPM1:SURF6N:rRNA droplets in buffer (top). **e**–**g**, ΔG^{tr} for coilin–eYFP (**e**), G3BP1 (**f**, −GFP empty, −mCherry filled), and DCP1A–eYFP (**g**) from the dilute phase (that is, nucleoplasm or cytoplasm) to Cajal bodies, arsenite-induced stress granules, and P-bodies (that is, dense phases), respectively. For all proteins here, a higher C^{dil} results from an increase in its expression (Fig. 1b, Extended Data Fig. 2a–c). AU, arbitrary units. Scale bars, 10 μm.

meshwork), their transfer free energy reports on the stability of interactions driving phase separation.

Applying this framework to our results for NPM1 (Fig. 1a, b) reveals that as the concentration of NPM1 is increased, the partition coefficient of NPM1 into the nucleolus decreases (Extended Data Fig. 1b); as such, the transfer free energy ΔG^{tr} for NPM1 between the condensed and the dilute phases becomes less negative, and thus destabilizing (Fig. 2c). This destabilizing effect at higher NPM1 concentrations implies that heterotypic—rather than homotypic (that is, NPM1–NPM1)—interactions dominate endogenous nucleolar assembly. To further test this conclusion, we focused on in vitro reconstitution of the nucleolar granular component. In addition to NPM1, key granular component biomolecules include ribosomal RNA (rRNA), multivalent proteins containing polyarginine motifs (Arg-proteins, such as SURF6) and ribosomal proteins (r-proteins). Using a well-established system for the phase separation of granular component biomolecules in vitro[11,12,20,23], we formed either NPM1-only droplets with 5% PEG as a crowder (Fig. 2d, bottom) or multicomponent droplets containing NPM1, the N terminus of SURF6 (SURF6N) and rRNA (Fig. 2d, top). As expected for single-biomolecule-component phase separation, as more NPM1 was added to the NPM1-only droplets, the transfer free energy remained roughly constant (Fig. 2d, green). By contrast, for multicomponent droplets, the transfer free energy became substantially less negative (that is, destabilizing) as more NPM1 was added, as was observed in living cells (Fig. 2d, black).

Notably, similar behaviour in cells was observed with numerous different intracellular condensates and their associated key scaffolding proteins: coilin in Cajal bodies, G3BP1 in arsenite-triggered stress granules and DCP1A in P-bodies. In each of these cases, increasing protein concentrations yielded larger condensates, surrounded by a higher C^{dil}, and with correspondingly less-negative transfer free energies (Fig. 2e–g, Extended Data Fig. 2); these data are consistent with previous studies that highlight the complex nature of biomolecule recruitment to in vitro- and in vivo-reconstituted condensates[12,24]. However, our findings contrast with the view that condensates are stabilized by predominantly homotypic interactions, for example those mediated by self-associating intrinsically disordered regions. Instead, the data suggest that heterotypic interactions have a central role in promoting the internal cohesivity that stabilizes LLPS—not only for nucleoli, but also for other intracellular condensates.

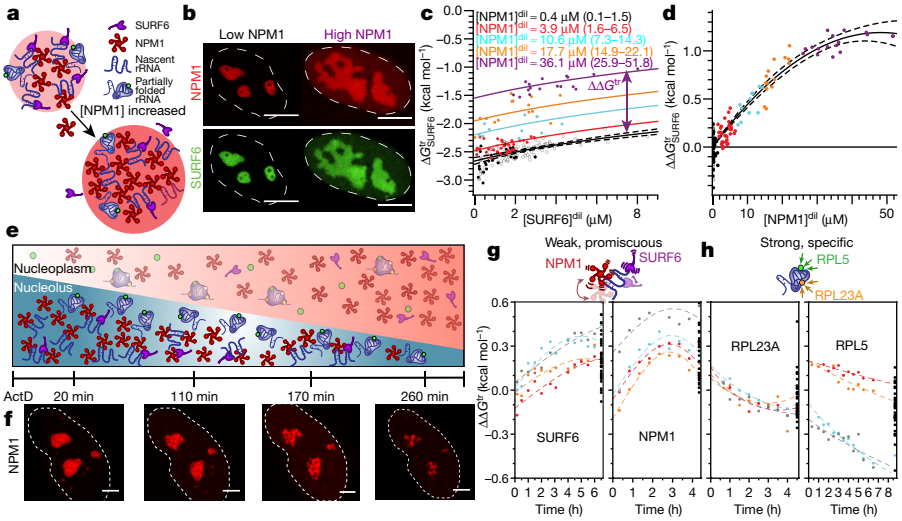

Fig. 3 | Heterotypic interactions between nucleolar proteins and rRNA underlie nucleolar thermodynamics. a, Schematic of the proposed mechanism for the dilution of non-NPM1 molecular interactions in the dense phase owing to NPM1 overexpression. Only relevant species are shown for clarity. **b**, Example images of cells (from $n = 102$ cells) expressing NPM1–mCherry (top) and SURF6–GFP (bottom) with low (left) and high (right) expression of NPM1. Scale bar, 10 μm. **c**, Change in the transfer free energy of SURF6 with overexpression of NPM1 plotted against the concentration of SURF6. The colours indicate different concentrations of NPM1 with mean and range values indicated; open circles are cells without additional NPM1 expressed. The method of calculating $\Delta\Delta G^{tr}$ at a referenced nucleoplasmic SURF6 concentration is shown via arrows and displaced lines in **c**. **d**, The change in ΔG^{tr} shown as a function of NPM1 concentration; the colour code is the same as in **c**. **e**, Schematic showing the effect of ActD treatment on nucleoli over time. **f**, Images of cells at the indicated times after ActD treatment (from $n = 4$ NPM1-tagged time series). The corresponding quantification for NPM1 cells is shown in Extended Data Fig. 5. Scale bars, 5 μm. **g**, **h**, $\Delta\Delta G^{tr}$ of SURF6 and NPM1 (**g**) and RPL23A and RPL5 (**h**) plotted against time after ActD treatment. Each colour represents an individual cell followed over time; black points are cells measured at the indicated time points. The schematics at the top of **g** and **h** highlight the differences in suggested interactions with rRNA.

We next investigated which heterotypic interactions drive phase separation of the nucleolus, by monitoring the transfer free energy of one component while changing the concentration of another (Fig. 3a). In our multicomponent in vitro mimic, we found that increasing the concentrations of NPM1 or SURF6N renders the partitioning of SURF6N less energetically favourable (Extended Data Fig. 4); this is again consistent with heterotypic interactions driving SURF6 to nucleoli. In living cells, SURF6 also exhibits behaviour similar to that of NPM1, with a destabilizing increase in the transfer free energy observed with increasing SURF6 concentration (Fig. 3c, black). This in vivo destabilization is markedly amplified with increasing NPM1 concentrations (Fig. 3b, c). From these data, we determined the change in ΔG^{tr} of SURF6 as a function of NPM1, by referencing to the energy expected without NPM1 overexpression—that is, $\Delta\Delta G^{tr}_{SURF6}([NPM1]^{dil}) = \Delta G^{tr}_{SURF6}([NPM1]^{dil}, [SURF6]^{dil}) - \Delta G^{tr}_{SURF6}([NPM1]^{dil} = 0, [SURF6]^{dil})$. Plotting $\Delta\Delta G^{tr}_{SURF6}$ against NPM1 collapses the data onto a single master curve (Fig. 3d, Supplementary Methods), highlighting a tight thermodynamic link between NPM1 and SURF6. This behaviour contrasts with that of r-proteins, which exhibit strong and specific rRNA binding, and a transfer free energy that is statistically insensitive to the concentration of NPM1 (Extended Data Fig. 5).

Both SURF6 and NPM1 have been proposed to interact with rRNA through weak promiscuous binding[12]. We therefore suggested that SURF6–NPM1 linkage occurs as a consequence of heterotypic interactions with rRNA, which are diluted upon NPM1 overexpression. To test whether heterotypic interactions with rRNA underlie the thermodynamics of nucleolar assembly, we performed our analysis in cells after treatment with actinomycin D (ActD), which is known to halt the transcription of nascent rRNA without affecting the processing and assembly of pre-existing rRNA[25,26] (Fig. 3e). As previously reported, the addition of ActD results in a progressive reduction of nucleolus size over the course of 4 hours[27] (Fig. 3f, Extended Data Fig. 6). Over time, the $\Delta\Delta G^{tr}$ of NPM1 and SURF6 increases, indicating weakened interactions relative to cells without ActD treatment. This is consistent with NPM1 and SURF6 driving heterotypic phase separation through multivalent interactions with nascent, unfolded (or misfolded) rRNA transcripts, which become increasingly scarce under ActD treatment. Conversely, we find that the two r-proteins RPL23A and RPL5 display the opposite behaviour—their transfer free energies decrease as ActD treatment progresses (Fig. 3g, h), reflecting strengthened interactions that are consistent with specific binding to more fully processed rRNA.

These findings shed light on how heterotypic interactions that drive phase separation facilitate sequential rRNA processing in ribosome biogenesis. Specifically, when compared with fully assembled ribosome subunits, relatively nascent rRNA transcripts are available for a greater number of interactions with NPM1, SURF6 and other scaffolding components of the granular component matrix, providing a mechanism to facilitate the vectorial flux of processed subunits out of the nucleolus[20] (Fig. 4f). Indeed, binding of nascent transcripts by r-proteins eliminates multivalent binding sites for heterotypic scaffolding proteins, which could serve to effectively expel fully assembled pre-ribosomal particles. We tested this concept using the biomimetic Corelet system—a 24-mer ferritin core in which each ferritin subunit is fused to an optogenetic heterodimerization domain that can be used to tune the effective valency of the particle with light[6] (Fig. 4a). We fused the optogenetic protein to an N-terminal-truncated construct of NPM1 (NPM1-C; residues 120–294), thereby allowing light-dependent multivalent interactions with the nucleolus. On its own, this construct partitions only weakly into nucleoli, with a ΔG^{tr} of approximately −0.4 kcal mol^{-1} (Extended Data Fig. 7). In the absence of bound NPM1-C, the ferritin core is strongly excluded from nucleoli with a ΔG^{tr} of approximately +1.4 kcal mol^{-1} (Extended Data Fig. 7); this is consistent with large non-interacting assemblies being excluded from the nucleolus and other condensates[28–30]. However, increasing the valence of the core by light activation results in an increase in its partitioning into the nucleolus, implying a more favourable (that is, negative) transfer free energy. This effect depends strongly on the valence of the core:

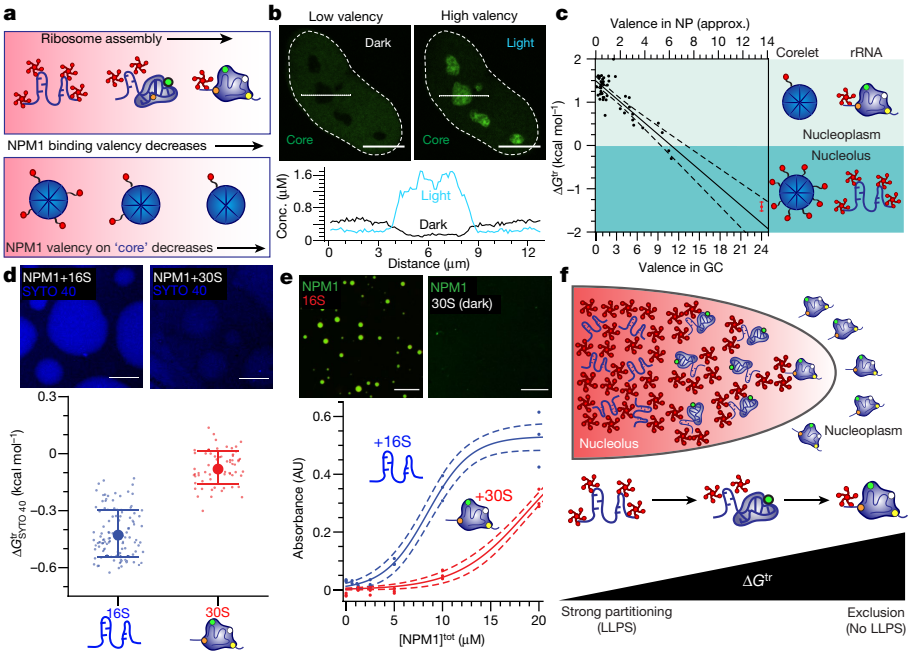

Fig. 4 | Composition-dependent heterotypic LLPS drives specific ribosomal subunit exclusion. a, Top, schematic of NPM1 valency as a function of rRNA folding and processing in the nucleolus; bottom, schematic of NPM1 valency on ferritin 'cores' using the Corelet optogenetic system. **b**, Images of a cell highlighting the partitioning of the cores before light exposure (low effective valence) (left) and after light exposure (high effective valence) (right), upon which NPM1-C binding sites on the core are saturated in this cell. Quantification is shown below, corresponding to the dashed line shown in the images. **c**, Corresponding quantification of the dependence of the ΔG^{tr} of the core on the valence in the granular component (GC) after light activation. Dotted lines are fits to data. NP, nucleoplasm. **d**, Top, representative images of 16S RNA (left) or the 30S small ribosomal subunit (right) partitioning into pre-formed 10 μM NPM1 droplets (made with 5% PEG-8K); the RNA species (used at 5 μg ml^{-1}) were visualized using 6.5 μM SYTO 40. Bottom, the corresponding transfer free energies of droplet formation. The large circles represent the mean and the error bars represent the standard deviation from $n = 118$ droplets (16S) and $n = 64$ droplets (30S). **e**, Top, microscopy images of 10 μM NPM1 incubated with 16S RNA (left) or the 30S small ribosomal subunit (right). Bottom, turbidity assay of NPM1 incubated at various concentrations with either 16S rRNA or the 30S small ribosomal subunit. The RNA species was added at 50 μg ml^{-1}; for validation of protein and RNA components see Extended Data Fig. 8. 16S rRNA was labelled via a morpholino approach as described in the Supplementary Methods. **f**, Proposed mechanism of ribosomal subunit exclusion from the granular component of the nucleolus driven by thermodynamics of nucleolar LLPS.

Corelets of valence less than 10 are excluded from the nucleolus ($\Delta G^{tr} > 0$), whereas those of valence greater than 10 are enriched ($\Delta G^{tr} < 0$) within the nucleolus (Fig. 4b, c, Extended Data Fig. 7). This physical picture is supported by in vitro experiments with NPM1 droplets and with ribosomal components of *Escherichia coli*, which reveal that ΔG^{tr} is more strongly negative for 16S rRNA compared with the 30S ribosomal subunit (comprising 16S plus associated r-proteins (Extended Data Fig. 8a–c)) (Fig. 4e). Consistent with these measurements, the in vitro phase separation of NPM1 is substantially weaker in the presence of the 30S subunit compared with 16S rRNA (Fig. 4d); this underscores how non-ribosomal protein bound (that is, smaller and highly solvent-exposed) rRNAs are associated with favourable heterotypic interactions that promote partitioning and phase separation with nucleolar scaffold proteins (Fig. 4d, e). Similarly, in vitro phase separation was substantially weaker in the presence of the full 70S ribosome compared with either 23S rRNA or total (that is, 23S, 16S and 5S) rRNA (Extended Data Fig. 8d). Taken together, these data suggest a mechanism in which phase separation of rRNA with the nucleolar scaffold becomes progressively less energetically favourable as components mature into fully assembled ribosomal subunits, leading to their thermodynamically driven exit from nucleoli.

Our findings lay the groundwork for a quantitative understanding of the interplay between the composition-dependent thermodynamics of condensate assembly and the free-energy landscape of biomolecular complex assembly. In particular, we show that heterotypic biomolecular interactions give rise to high-dimensional phase behaviour that yields C_{sat} values that vary with component concentrations, providing a mechanism for tuning condensate composition. This enables 'on demand' condensate assembly—such that phase separation occurs only in the presence of the substrate—while simultaneously enabling a non-equilibrium steady-state flux of products (substrates), which are driven out of (or in to) the condensate during processing. This is likely to be relevant not only to the nucleolus, but also to many other phase-separated condensates that facilitate the formation of diverse biomolecular complexes, such as the spliceosome. Future work will exploit these intracellular thermodynamic self-assembly principles towards new organelle-engineering applications.

Online content

Any methods, additional references, Nature Research reporting summaries, source data, extended data, supplementary information, acknowledgements, peer review information; details of author contributions and competing interests; and statements of data and code availability are available at https://doi.org/10.1038/s41586-020-2256-2.

1. Shin, Y. & Brangwynne, C. P. Liquid phase condensation in cell physiology and disease. *Science* **357**, eaaf4382 (2017).
2. Banani, S. F., Lee, H. O., Hyman, A. A. & Rosen, M. K. Biomolecular condensates: organizers of cellular biochemistry. *Nat. Rev. Mol. Cell Biol.* **18**, 285–298 (2017).
3. Nott, T. J. et al. Phase transition of a disordered nuage protein generates environmentally responsive membraneless organelles. *Mol. Cell* **57**, 936–947 (2015).
4. Shin, Y. et al. Spatiotemporal control of intracellular phase transitions using light-activated optoDroplets. *Cell* **168**, 159–171.e14 (2017).
5. Wang, J. et al. A molecular grammar governing the driving forces for phase separation of prion-like RNA binding proteins. *Cell* **174**, 688–699.e16 (2018).
6. Bracha, D. et al. Mapping local and global liquid phase behavior in living cells using photo-oligomerizable seeds. *Cell* **175**, 1467–1480.e13 (2018).

7. Holehouse, A. S. & Pappu, R. V. Functional implications of intracellular phase transitions. *Biochemistry* **57**, 2415–2423 (2018).
8. Alberti, S., Gladfelter, A. & Mittag, T. Considerations and challenges in studying liquid-liquid phase separation and biomolecular condensates. *Cell* **176**, 419–434 (2019).
9. McSwiggen, D. T., Mir, M., Darzacq, X. & Tjian, R. Evaluating phase separation in live cells: diagnosis, caveats, and functional consequences. *Genes Dev*. **33**, 1619–1634 (2019).
10. Oltsch, F., Klosin, A., Julicher, F., Hyman, A. A. & Zechner, C. Phase separation provides a mechanism to reduce noise in cells. *Science* **367**, 464–468 (2019).
11. Feric, M. et al. Coexisting liquid phases underlie nucleolar subcompartments. *Cell* **165**, 1686–1697 (2016).
12. Mitrea, D. M. et al. Nucleophosmin integrates within the nucleolus via multi-modal interactions with proteins displaying R-rich linear motifs and rRNA. *eLife* **5**, e13571 (2016).
13. Flory, P. J. *Principles of Polymer Chemistry* (Cornell Univ. Press, 1953).
14. Wei, M.-T., Chang, Y.-C., Shimobayashi, S. F., Shin, Y. & Brangwynne, C. P. Nucleated transcriptional condensates amplify gene expression. Preprint at https://www.biorxiv.org/content/10.1101/737387v2 (2019).
15. Kedersha, N. et al. G3BP–Caprin1–USP10 complexes mediate stress granule condensation and associate with 40S subunits. *J. Cell Biol*. **212**, e201508028 (2016).
16. Choi, J.-M., Dar, F. & Pappu, R. V. LASSI: A lattice model for simulating phase transitions of multivalent proteins. *PLoS Comput. Biol*. **15**, e1007028 (2019).
17. Mao, S., Kuldinow, D., Haataja, M. P. & Košmrlj, A. Phase behavior and morphology of multicomponent liquid mixtures. *Soft Matter* **15**, 1297–1311 (2019).
18. Priftis, D. & Tirrell, M. Phase behaviour and complex coacervation of aqueous polypeptide solutions. *Soft Matter* **8**, 9396–9405 (2012).
19. Jacobs, W. M. & Frenkel, D. Phase transitions in biological systems with many components. *Biophys. J*. **112**, 683–691 (2017).
20. Mitrea, D. M. et al. Self-interaction of NPM1 modulates multiple mechanisms of liquid–liquid phase separation. *Nat. Commun*. **9**, 842 (2018).
21. Lin, Y.-H., Brady, J. P., Forman-Kay, J. D. & Chan, H. S. Charge pattern matching as a 'fuzzy' mode of molecular recognition for the functional phase separations of intrinsically disordered proteins. *New J. Phys*. **19**, 115003 (2017).
22. Banerjee, P. R., Milin, A. N., Moosa, M. M., Onuchic, P. L. & Deniz, A. A. Reentrant phase transition drives dynamic substructure formation in ribonucleoprotein droplets. *Angew. Chem. Int. Ed*. **56**, 11354–11359 (2017).
23. Ferrolino, M. C., Mitrea, D. M., Michael, J. R. & Kriwacki, R. W. Compositional adaptability in NPM1–SURF6 scaffolding networks enabled by dynamic switching of phase separation mechanisms. *Nat. Commun*. **9**, 5064 (2018).
24. Banani, S. F. et al. Compositional control of phase-separated cellular bodies. *Cell* **166**, 651–663 (2016).
25. Geuskens, M. & Bernhard, W. Cytochimie ultrastructurale du nucléole. 3. Action de l'actinomycine D sur le métabolisme du RNA nucléolaire. *Exp. Cell Res*. **44**, 579–598 (1966).
26. Lazdins, I. B., Delannoy, M. & Sollner-Webb, B. Analysis of nucleolar transcription and processing domains and pre-rRNA movements by in situ hybridization. *Chromosoma* **105**, 481–495 (1997).
27. Burger, K. et al. Chemotherapeutic drugs inhibit ribosome biogenesis at various levels. *J. Biol. Chem*. **285**, 12416–12425 (2010).
28. Wei, M.-T. et al. Phase behaviour of disordered proteins underlying low density and high permeability of liquid organelles. *Nat. Chem*. **9**, 1118–1125 (2017).
29. Zhu, L. et al. Controlling the material properties and rRNA processing function of the nucleolus using light. *Proc. Natl Acad. Sci. USA* **116**, 17330–17335 (2019).
30. Handwerger, K. E., Cordero, J. A. & Gall, J. G. Cajal bodies, nucleoli, and speckles in the *Xenopus* oocyte nucleus have a low-density, sponge-like structure. *Mol. Biol. Cell* **16**, 202–211 (2005).

Reporting summary

Further information on research design is available in the Nature Research Reporting Summary linked to this paper.

Data availability

Source data for Figs. 1–4 and Extended Data Figs. 1, 2, 3, 4–8 are available with the paper. All other data are available from the corresponding authors upon reasonable request.

Acknowledgements We thank members of the Brangwynne laboratory for discussions and comments on this manuscript. This work was supported by the Howard Hughes Medical Institute, the St Jude Collaborative on Membraneless Organelles, and grants from the National Institutes of Health (NIH) 4D Nucleome Program (U01 DA040601) and the Princeton Center for Complex Materials, a Materials Research Science and Engineering Center supported by the National Science Foundation (NSF) (DMR 1420541). L.Z. was supported by an NSF graduate fellowship (DGE-1656466). R.W.K acknowledges support from the NIH (R01 GM115634, R35 GM131891 and P30 CA021765 (to St Jude Children's Research Hospital)) and ALSAC. M.T. acknowledges support from the NIH (F32 GM131524). Some images were acquired at the St Jude Cell & Tissue Imaging Center, which is supported by St Jude Children's Research Hospital and the National Cancer Institute (P30 CA021765); we thank V. Frohlich and J. Peters for technical assistance.

Author contributions J.A.R., L.Z., D.M.M., R.W.K. and C.P.B. designed the research; in vivo studies were performed and analysed by J.A.R., L.Z., D.W.S. and M.W.; in vitro studies were performed and analysed by M.C.F., M.T. and D.M.M.; J.A.R., L.Z. and C.P.B. wrote the manuscript, which was reviewed and edited by all authors.

Competing interests R.W.K. is a consultant for, and D.M.M. has recently become employed by, Dewpoint Therapeutics. The remaining authors declare no competing interests.

Additional information
Supplementary information is available for this paper at https://doi.org/10.1038/s41586-020-2256-2.
Correspondence and requests for materials should be addressed to R.W.K. or C.P.B.
Peer review information *Nature* thanks Rohit Pappu and the other, anonymous, reviewer(s) for their contribution to the peer review of this work.
Reprints and permissions information is available at http://www.nature.com/reprints.

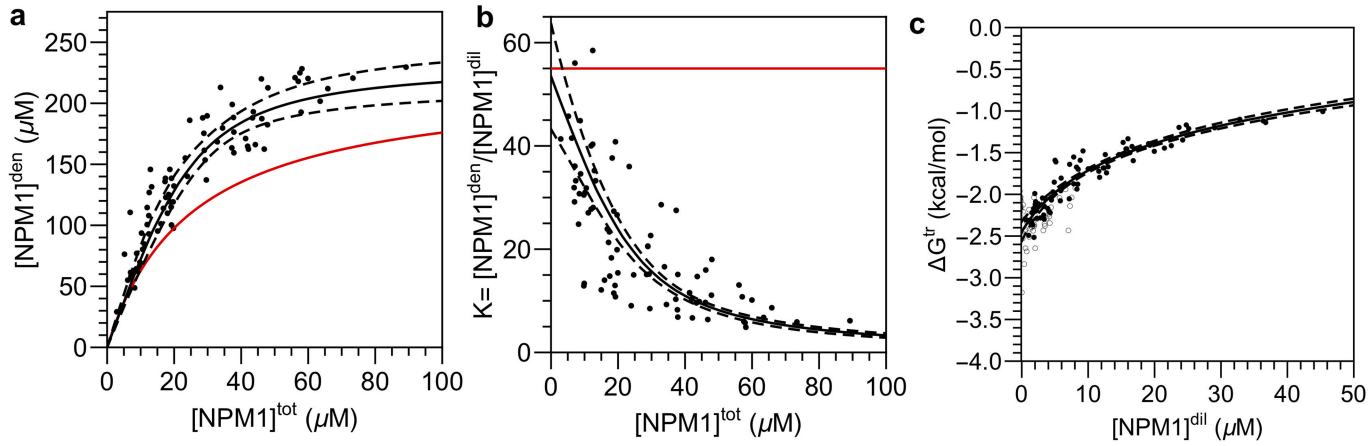

Extended Data Fig. 1 | NPM1 lacks a fixed C^{dil} and C^{den}, suggesting that nucleoli undergo multicomponent-mediated phase separation. **a**, **b**, Dependence of the measured concentration of NPM1 in the relevant dense phase (here 'den' refers to the granular component of nucleoli) (**a**) and the apparent partition coefficient of NPM1 (that is, the ratio of its concentration in the dense and dilute phases) (**b**) on the total concentration of NPM1 in the nucleus. **c**, Dependence of the transfer free energy on the concentration of NPM1 in the dilute phase, for mCherry-tagged NPM1 (filled circles) and mGFP-tagged (open circles). The trends for each are similar. Dashed lines represent mean confidence intervals to fits described in the Supplementary Methods; the red lines in **a**, **b** represent expected trends for single-biomolecule phase separation.

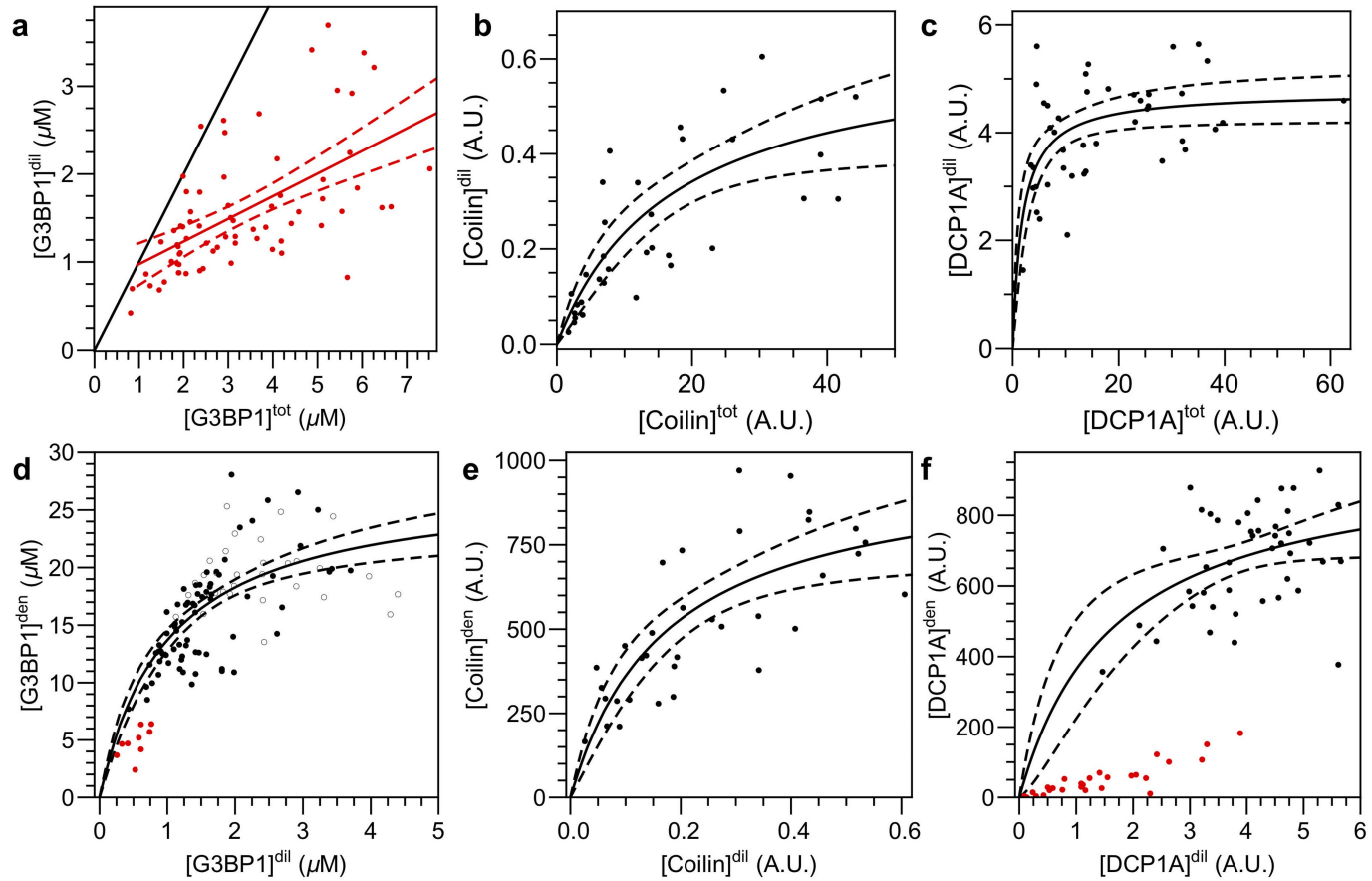

Extended Data Fig. 2 | G3BP1, coilin and DCP1A lack fixed C^{dil} and C^{den} in cells. a–**c**, Relationship between the approximated total concentration and the dilute concentration in cells expressing variable amounts of fluorescently tagged G3BP1 (**a**), coilin (**b**) and DCP1A (**c**). Points are red in **a** to indicate that only cells with phase separation in the G3BP1 double knockout line after stress are included. **d**–**f**, Relationship between the dilute and dense concentrations for cells expressing variable amounts of fluorescently tagged G3BP1 (**d**), coilin (**e**) and DCP1A (**f**). Dashed lines represent mean confidence intervals to fits described in the Supplementary Methods. Statistical significance ($P < 0.01$) for these increasing monotonic relationships between the axes are reported in Supplementary Methods. Red points in **d** and **f** represent diffraction-limited foci.

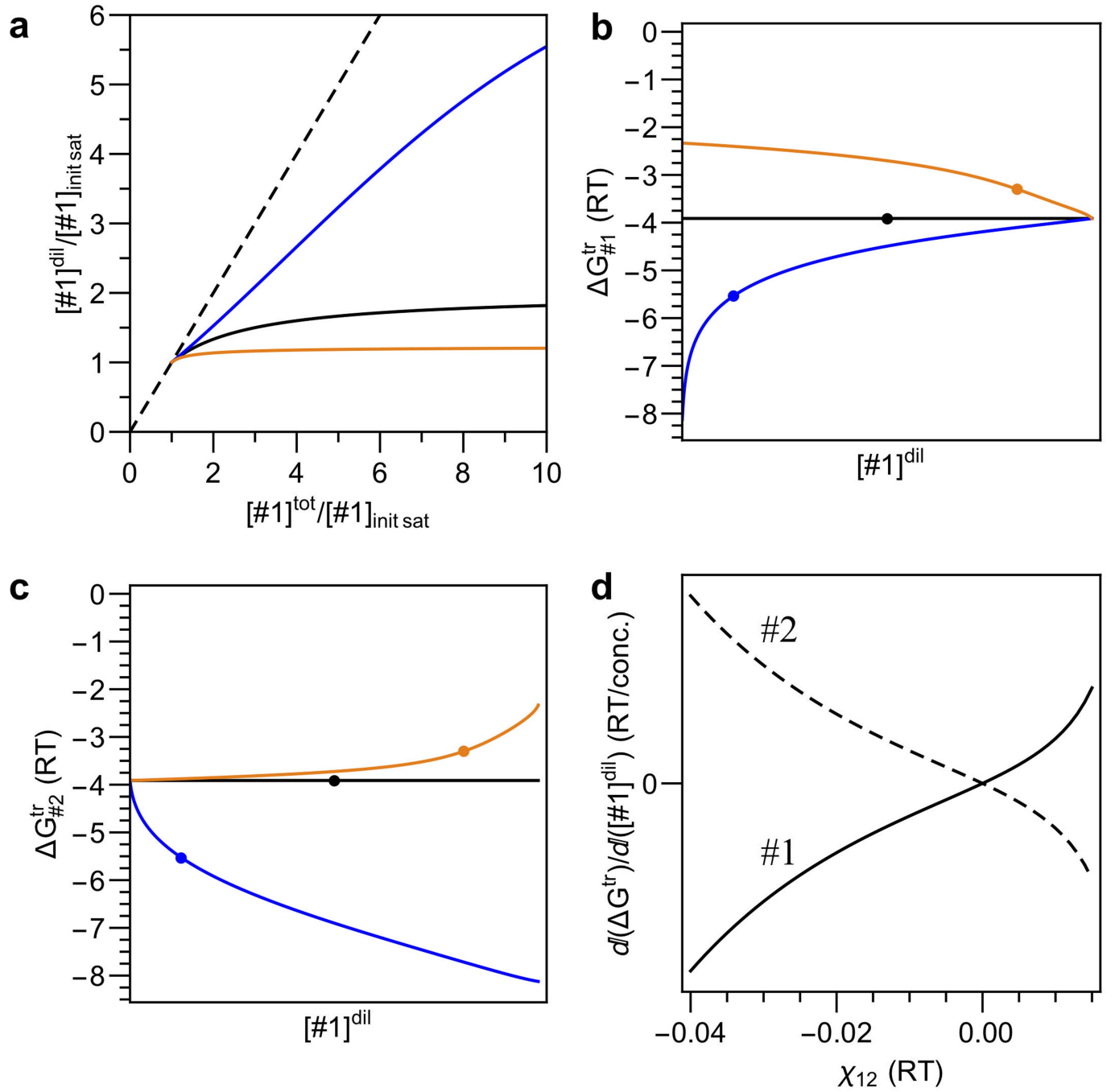

Extended Data Fig. 3 | In silico validation of the composition dependence of phase separation using Flory–Huggins theory. Phase separation of two (non-solvent) components, denoted #1 and #2, with their heterotypic interactions being equal, stronger and weaker, than their homotypic interactions shown as black, blue and orange, respectively, for **a**–**c**. **a**, The initial dependence of $[\#1]^{dil}$ on $[\#1]^{tot}$ at fixed $[\#2]^{tot}$, such that phase separation will occur at the 'goldilocks point'—when $[\#1]^{tot} = [\#2]^{tot}$. The axes are normalized by the initial saturation (init sat) concentration—that is, the lowest $[\#1]^{tot}$ at which phase separation emerges. The dashed line is the 1:1 line that would expected without phase separation. **b**, **c**, $\Delta G^{tr}_{\#1}$ (**b**) and $\Delta G^{tr}_{\#2}$ (**c**) as a function of $[\#1]^{dil}$. Circles indicate the location of the goldilocks point under each condition. **d**, The change in ΔG^{tr} with respect to $[\#1]^{dil}$ as a function of the heterotypic interaction strength χ_{12} (in which more negative implies stronger heterotypic interactions) at the goldilocks point for the transfer free energy of #1 and #2, as indicated.

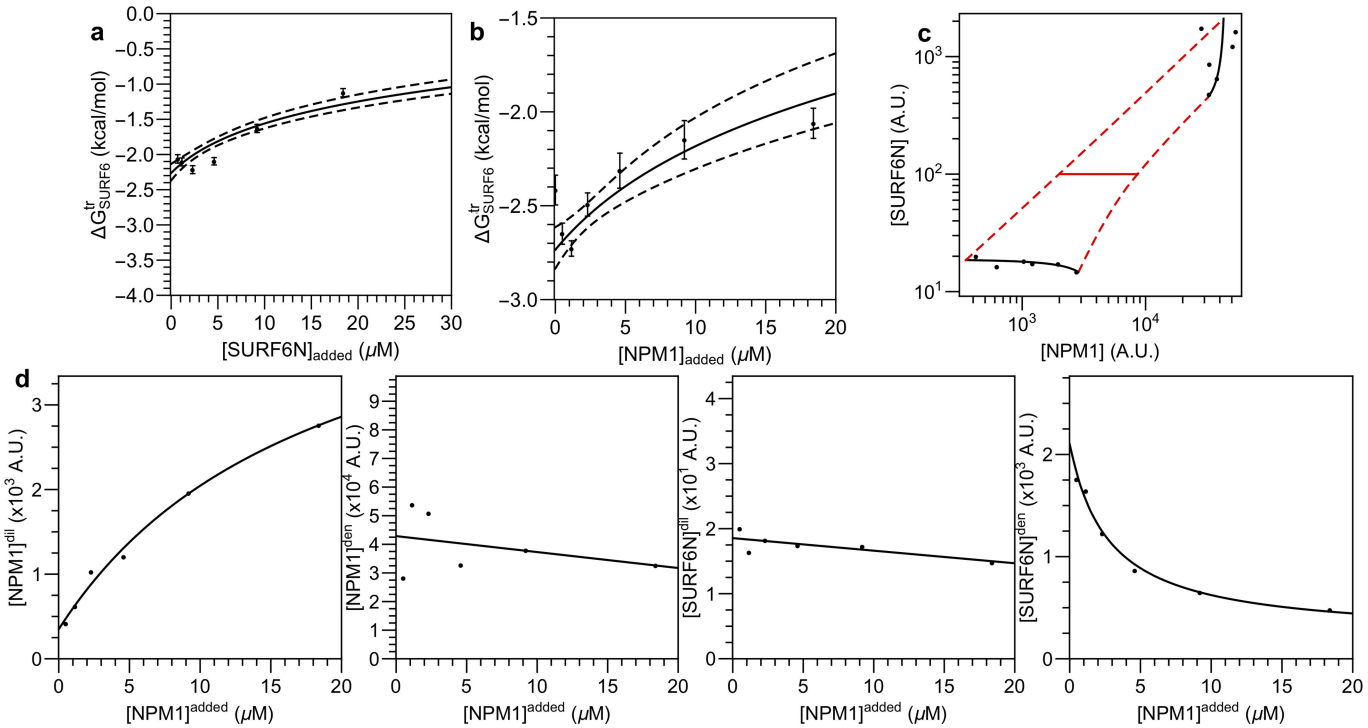

Extended Data Fig. 4 | In vitro destabilization of SURF6N partitioning by increasing the concentration of SURF6N itself or NPM1. a, **b**, Changes in the transfer free energy of SURF6N forming into multicomponent droplets as additional SURF6N (**a**) or additional NPM1 (**b**) is added on top of NPM1:SURF6N:rRNA ternary droplets as described in the Supplementary Methods. The number of droplets (in order of increasing concentration) are $n = 122, 115, 105, 98, 91, 74$ and 99. Data are mean ± s.d. **c**, Phase diagram in vitro in the presence of 25 ng μl^{-1} wheatgerm rRNA, 5 μM SURF6N, and various concentrations of NPM1. Units shown are absorbance units corrected for background, quantum yield differences between the two phases, and the (nonlinear) fraction labelled of NPM1. **d**, Changes in the phase diagram as additional NPM1 is added. As in **c**, NPM1 concentrations in the dense or dilute phases are indicative of total NPM1. Hyperbolic fits shown highlight that the largest changes upon NPM1 addition are from an increase in the dilute phase concentration of NPM1 and a decrease in the dense phase concentration of SURF6N. To assess significance, the *y* axes in **d** are shown from zero arbitrary units (AU) to 2.5 times the mean of all points shown.

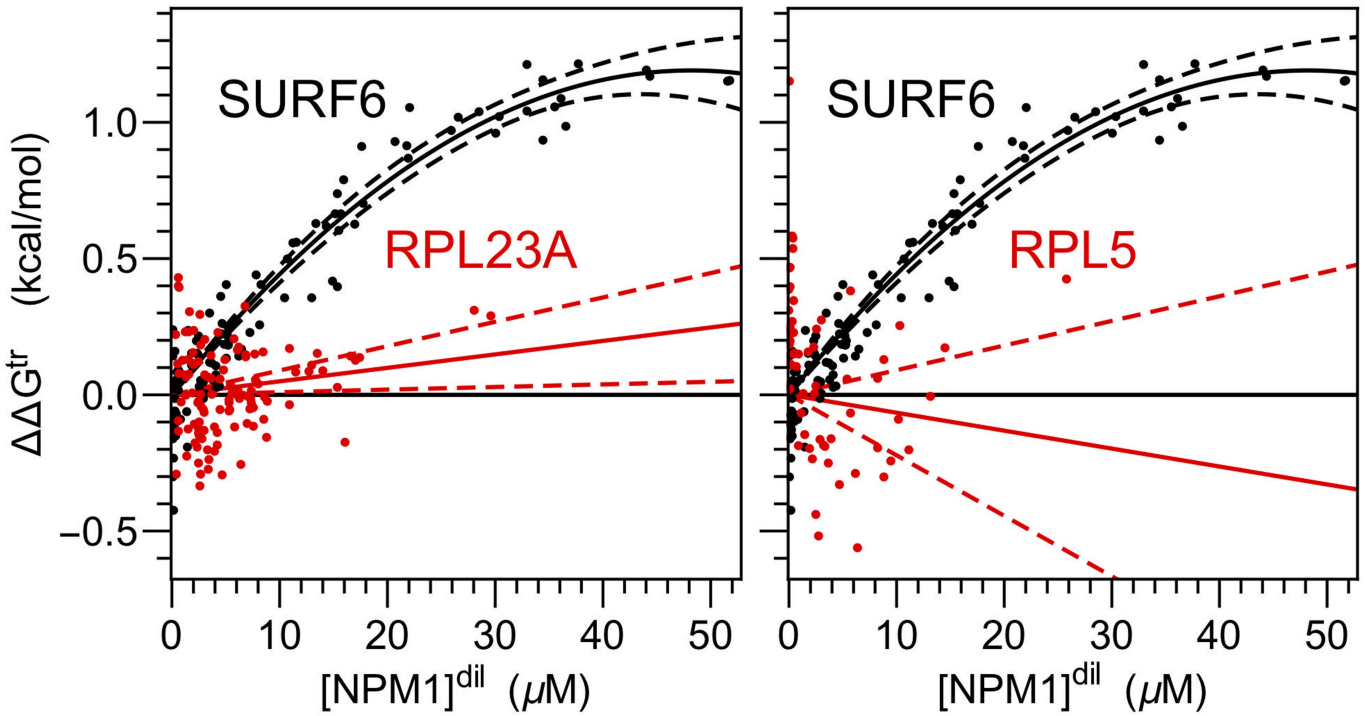

Extended Data Fig. 5 | The change in the transfer free energy for R-proteins and NPM1. $\Delta\Delta G^{tr}$ of r-proteins RPL23A (left) and RPL5 (right) compared with that for SURF6 as the concentration of NPM1 is increased.

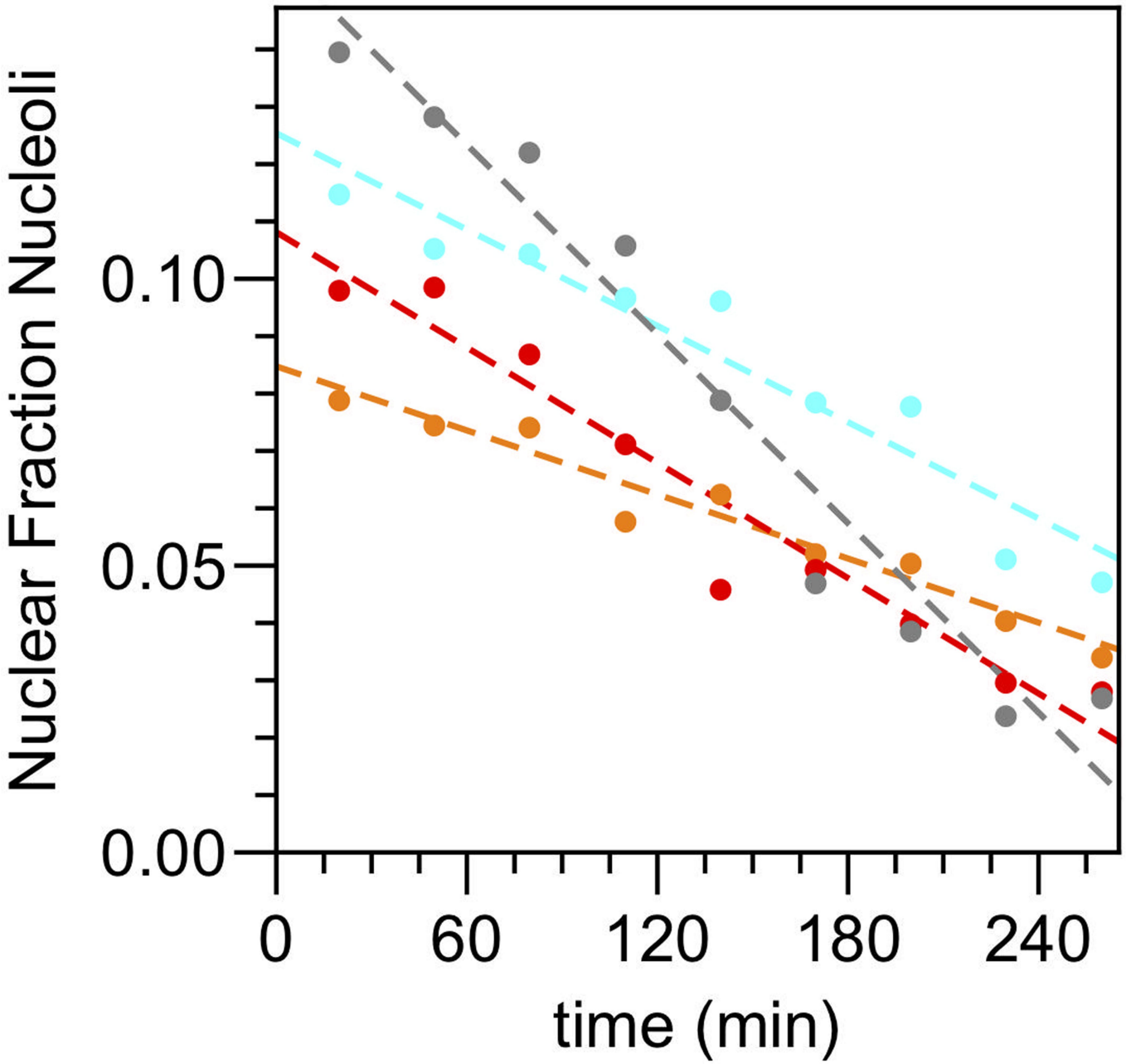

Extended Data Fig. 6 | ActD treatment decreases the size of the nucleolus. The fraction of the image area corresponding to the nucleolus as a function of time after the addition of ActD in individual cells expressing NPM1–mCherry. The colours represent the same cells as in Fig. 3g.

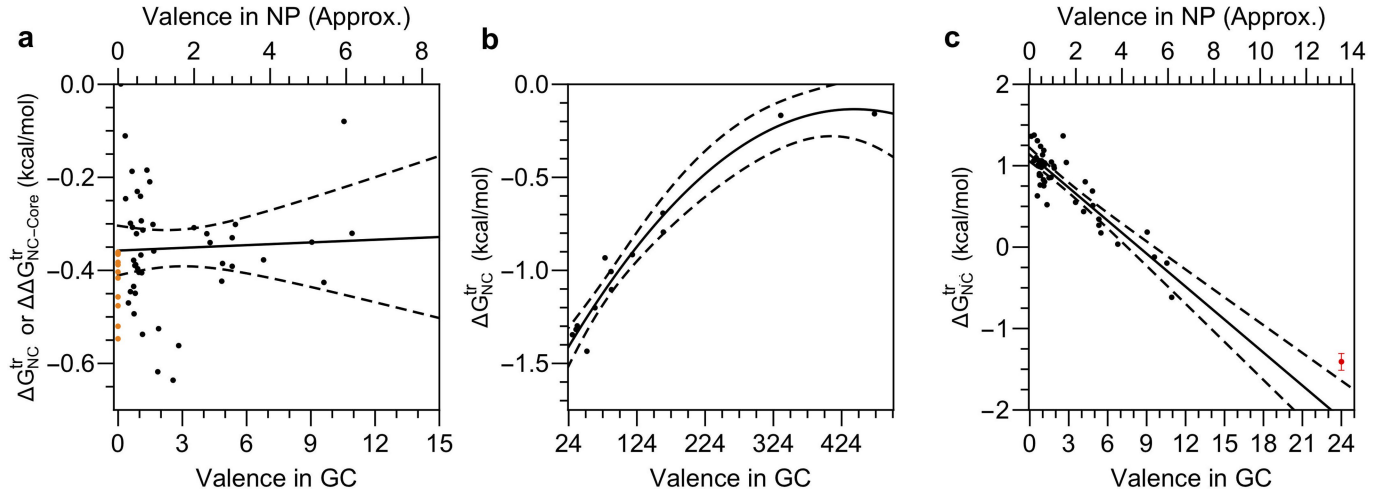

Extended Data Fig. 7 | Characterization of Corelet non-ideality and extrapolation from high valence. a, The transfer free energy for the N-terminal half of NPM1 (NC)-sspB in cells without the core expressed (orange representing ΔG^{tr}) or with the indicated valences after core activation (black indicating $\Delta\Delta G^{tr}_{NC\text{-}Core}$). The $\Delta\Delta G^{tr}_{NC\text{-}Core}$ in this case is the energetic difference between the NC and core channels, which is approximately the energetic difference for transferring an additional NC to the core at that valence. **b**, At valences higher then 24, the transfer free energy is approximated as quadratic and extrapolated back to a valence of 24 to obtain the transfer free energy at this valence. **c**, Transfer free energy reported from the sspB channel as a function of valence, which is weighted by the number of sspB molecules (owing to the number of mCherry molecules observed being proportional to the valence of each molecule, as opposed to at the core where it is always constant at 24 GFPs). The red point represents the extrapolated value and mean confidence error as determined in **b**.

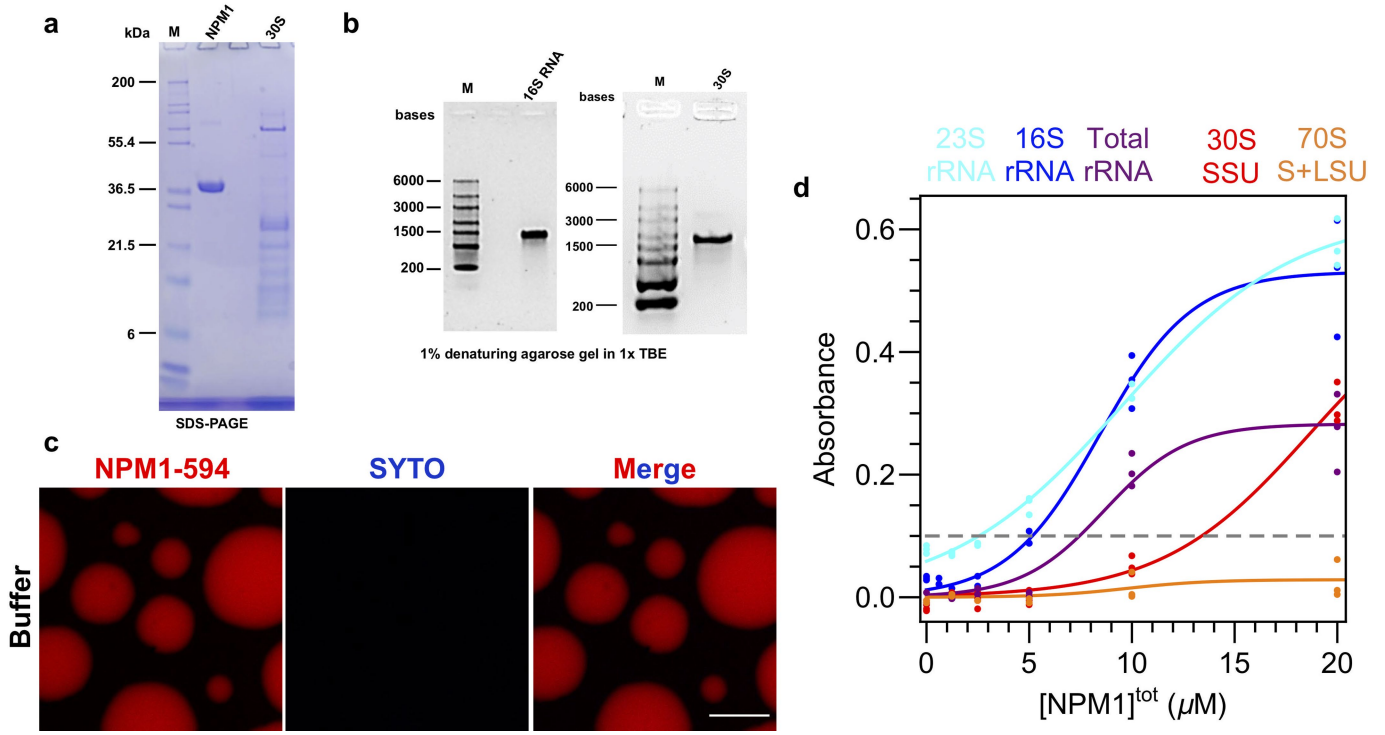

Extended Data Fig. 8 | Controls for ribosomal mimics. a, **b**, SDS–PAGE (**a**) and denaturing agarose gel (**b**) detailing the purity of reagents used in the experiments in Fig. 4d, e. **c**, Microscopy image of 10 µM NPM1-594 droplets formed with 5% PEG without any rRNA. The limited fluorescence indicates that neither NPM1 nor PEG binds SYTO 40 and the droplet environment does not promote the fluorescence of SYTO 40. **d**, Phase separation assessed by turbidity of the indicated ribosomal substrate (fixed at 50 µg ml^{-1}) as a function of NPM1 concentration. The dashed grey line indicates where phase separation is typically observed in microscopy measurements.

nature research

Corresponding author(s): Clifford P. Brangwynne

Last updated by author(s): Mar 20, 2020

Reporting Summary

Nature Research wishes to improve the reproducibility of the work that we publish. This form provides structure for consistency and transparency in reporting. For further information on Nature Research policies, see Authors & Referees and the Editorial Policy Checklist.

Statistics

For all statistical analyses, confirm that the following items are present in the figure legend, table legend, main text, or Methods section.

n/a	Confirmed	
☒	☐	The exact sample size (*n*) for each experimental group/condition, given as a discrete number and unit of measurement
☒	☐	A statement on whether measurements were taken from distinct samples or whether the same sample was measured repeatedly
☐	☒	The statistical test(s) used AND whether they are one- or two-sided *Only common tests should be described solely by name; describe more complex techniques in the Methods section.*
☒	☐	A description of all covariates tested
☒	☐	A description of any assumptions or corrections, such as tests of normality and adjustment for multiple comparisons
☒	☐	A full description of the statistical parameters including central tendency (e.g. means) or other basic estimates (e.g. regression coefficient) AND variation (e.g. standard deviation) or associated estimates of uncertainty (e.g. confidence intervals)
☒	☐	For null hypothesis testing, the test statistic (e.g. *F*, *t*, *r*) with confidence intervals, effect sizes, degrees of freedom and *P* value noted *Give P values as exact values whenever suitable.*
☒	☐	For Bayesian analysis, information on the choice of priors and Markov chain Monte Carlo settings
☒	☐	For hierarchical and complex designs, identification of the appropriate level for tests and full reporting of outcomes
☒	☐	Estimates of effect sizes (e.g. Cohen's *d*, Pearson's *r*), indicating how they were calculated

Our web collection on statistics for biologists contains articles on many of the points above.

Software and code

Policy information about availability of computer code

Data collection	Nikon Elements was used to collect data.
Data analysis	Data was analyzed as described in the Methods.

For manuscripts utilizing custom algorithms or software that are central to the research but not yet described in published literature, software must be made available to editors/reviewers. We strongly encourage code deposition in a community repository (e.g. GitHub). See the Nature Research guidelines for submitting code & software for further information.

Data

Policy information about availability of data

All manuscripts must include a data availability statement. This statement should provide the following information, where applicable:

- Accession codes, unique identifiers, or web links for publicly available datasets
- A list of figures that have associated raw data
- A description of any restrictions on data availability

Source data for Figures 1-4 and Extended Data Figures 1, 2, 3–8 are available with the paper. All other data are available from the corresponding authors upon request.

Field-specific reporting

Please select the one below that is the best fit for your research. If you are not sure, read the appropriate sections before making your selection.

☒ Life sciences ☐ Behavioural & social sciences ☐ Ecological, evolutionary & environmental sciences

Life sciences study design

All studies must disclose on these points even when the disclosure is negative.

Sample size	At least two dozen or more data points were collected across the largest experimentally possible dynamic range consistent with ideal practice for biophysical research.
Data exclusions	No data were excluded from the analyses except when condensate was below the diffraction limit. This exclusion was predetermined as concentrations of objects below the diffraction limit are immeasurable in standard confocal microscopy.
Replication	All attempts at replication were successful.
Randomization	No randomization was preformed as experiments within the study have been highly reproducible (e.g. day to day, locations used on multi-well plate) and often additional data points are collected as a consequence of the previous data (e.g. cells failed to express enough protein).
Blinding	Investigators were not blinded as analysis is required to assure expression levels span required dynamic range as is typical for biophysical experiments.

Reporting for specific materials, systems and methods

We require information from authors about some types of materials, experimental systems and methods used in many studies. Here, indicate whether each material, system or method listed is relevant to your study. If you are not sure if a list item applies to your research, read the appropriate section before selecting a response.

Materials & experimental systems

n/a	Involved in the study
☒	☐ Antibodies
☐	☒ Eukaryotic cell lines
☒	☐ Palaeontology
☒	☐ Animals and other organisms
☒	☐ Human research participants
☒	☐ Clinical data

Methods

n/a	Involved in the study
☒	☐ ChIP-seq
☒	☐ Flow cytometry
☒	☐ MRI-based neuroimaging

Eukaryotic cell lines

Policy information about cell lines

Cell line source(s)	HeLa cells were obtained from ATCC. U2OS G3BP1/2 KO cells were previously described (Kedersha et al., 2016).
Authentication	None of the cell lines used were authenticated.
Mycoplasma contamination	All cell lines tested negative for mycoplasma contamination.
Commonly misidentified lines (See ICLAC register)	None.